

Atmospheric effects in satellite imaging of mountainous terrain

Robert W. Sjöberg and Berthold K. P. Horn

It is possible to obtain useful maps of surface albedo from remotely sensed images by eliminating effects due to topography and the atmosphere, even when the atmospheric state is not known. A simple phenomenological model of earth radiance that depends on six empirically determined parameters is developed given certain simplifying assumptions. The model incorporates path radiance and illumination from sun and sky and their dependencies on surface altitude and orientation. It takes explicit account of surface shape, represented by a digital terrain model, and is therefore especially suited for use in mountainous terrain. A number of ways of determining the model parameters are discussed, including the use of shadows to obtain path radiance and to estimate local albedo and sky irradiance. The emphasis is on extracting as much information from the image as possible, given a digital terrain model of the imaged area and a minimum of site-specific atmospheric data. The albedo image, introduced as a representation of surface reflectance, provides a useful tool to evaluate the simple imaging model. Criteria for the subjective evaluation of albedo images are established and illustrated for Landsat multispectral data of a mountainous region of Switzerland. The method exposes some of the limitations found in computing reflectance information using only the image-forming equation.

I. Introduction

Earth-sensing satellites are widely used to help map natural resources, a very large fraction of which are concentrated in mountainous terrain. Such areas are often inaccessible to direct survey methods, and one must rely on remote sensing to provide needed information. Since there are insufficient skilled photogrammetrists to handle the vast quantity of satellite data made possible through such programs as Landsat, automated preprocessing is essential. The development of computational schemes to help automate the interpretation process requires an understanding of the imaging process.

The acquisition of information about mountainous terrain is important, but there have been relatively few successful applications of remotely sensed images for such areas. Explicit slope and elevation data have been used several times as separate channels in automated classification.¹⁻³ Hoffer and his co-workers were among the first to at least recognize the role of cast shadows in images of rugged topography.² Later studies have

recognized the role of slope and elevation in the imaging process. Shadovsky and Malila⁴ used slope information to account for foreshortening and self-shadow. A recent paper by Holben and Justice⁵ described field experiments and satellite simulations to explicitly study the topographic effect on remote imaging. The simulations were, however, specifically designed to minimize and ignore atmospheric interactions by assuming clear sky conditions and concentrating on spectral channels in which the atmospheric effects are not normally significant.

The goal of multispectral remote sensing is to recover information about the imaged scene. This information is usually surface reflectance, an intrinsic property of the material comprising the surface that is independent of the particulars of illumination, topography, and sensor position. Reliable recovery of reflectance demands an accurate model of the imaging process, embodied in what is called the image-forming or image irradiance equation. This equation relates image irradiance to local surface reflectance, incident illumination, optical properties of the sensor, and other radiometric quantities. To compute the desired surface description as a function of image irradiance and other parameters, it is necessary to invert the image-forming equation.

Inverting the image-forming equation is a difficult task in high-altitude satellite sensing of the earth due to the presence of the atmosphere. The atmosphere affects satellite imaging in at least three ways that must

The authors are with Massachusetts Institute of Technology, Artificial Intelligence Laboratory, Cambridge, Massachusetts 02139.

Received 17 May 1982.

0003-6935/83/111702-15\$01.00/0.

© 1983 Optical Society of America.

be accounted for in the imaging equation: it attenuates energy passing through, it confounds the desired signal with irrelevant or spurious path radiance, and it imposes a distributed surface illuminant in the form of skylight. A substantial literature has developed on the relationship of atmospheric optics to remote sensing. A sample of that literature can be found in the extensive bibliography of Howard and Garing.⁶ The reader is referred to McCartney's book on atmospheric optics⁷ and Rozenberg's treatise on light scattering⁸ for introductory material. LaRocca and Turner⁹ have published a comprehensive state-of-the-art review of methods for computing atmospheric quantities applicable to remote sensing.

The interaction of atmospheric effects with those of topography makes remote sensing in mountainous terrain especially difficult. One effect results from variations in elevation across the scene. The air mass between the sensor and the surface diminishes with altitude, and atmospheric effects are consequently reduced. There is less attenuation of solar illumination and reflected radiance, less skylight, and less extraneous path radiance at higher altitude. Another effect is due to wide variation in surface orientation across the scene. The slope of a surface element determines its exposure to sunlight and skylight. An element that slopes away from the sun sufficiently is self-shadowed and receives no sunlight. Even surfaces that would otherwise be sunlit may lie in shadows cast by surrounding terrain features. Shadows are abundant in Landsat images of mountainous regions due to the low solar elevation resulting from the early morning overflight time. By modeling the contribution of skylight to the reflected surface radiance, it is possible to recover information about the ground even in shadows.

The thrust of the research reported in this paper was to render a more faithful representation of surface reflectance than an original satellite image can deliver by explicitly accounting for elevation and slope variation and atmospheric effects within the scene. The three goals of the research were (1) to develop a computationally simple form of the image-forming equation suitable when viewing rough terrain through an atmosphere; (2) to explore ways of determining the model parameters directly from a satellite image when a minimum of site-specific data is available; and (3) to present the albedo map as a representation of surface reflectance and to evaluate it as a tool in determining model parameters.

An albedo image or albedo map is a synthetic image that characterizes the reflectance at each point on the surface by a single scalar value. This is possible under certain circumstances (such as assuming a Lambertian surface) since the only difference in reflectance of any two points is the difference in the relative amounts of incident energy reflected from each. The albedo represents an intrinsic property of the terrain cover and should be invariant with respect to terrain shape, sun and sensor position, and atmospheric state. Several albedo images from different spectral channels can be combined to produce a false-color map of terrain cover.

The composite albedo data may also be fed to a pattern classification system. Since the albedo map more closely represents surface properties than the raw image, better classification results are expected, although this particular extension was not explored.

An albedo map can be generated only after the image-forming equation has been inverted to express local albedo in terms of topographic, atmospheric, and sensor optical properties. Effects due to the sensor itself are presumably known. Those due to topography can be determined from a suitable digital terrain model of the area imaged. Atmospheric effects, on the other hand, are not easily ascertained. A complete treatment involves the solution of the 3-D nonlinear integro-differential radiative transfer equation appropriate to a spherical earth.⁹⁻¹² This is computationally infeasible, even if the required information were available.

A number of assumptions simplify the sensor radiance equation to one depending on only six parameters. These parameters are empirically determined from the image and auxiliary data. Without site-specific information, however, it is difficult to obtain trustworthy values.

A trial-and-error approach is explored here. An albedo image is generated using a trial set of model parameters and evaluated according to subjective criteria of acceptability. Adjustments are made in the values of the parameters, another albedo image is produced, and the evaluation is repeated. Although no formalism for determining an optimal albedo image is given, experiments indicate that satisfactory results can be obtained.

II. Sensor Radiance Equation

A. Image-Forming Equation

The signal generated by a remote imaging system depends on the irradiance striking the photosensitive surface of the sensor. It is assumed that the characteristics of the optical system are known sufficiently well that one can recover this irradiance from the signal by inverting the sensor's transfer function. For a small aperture, the sensor irradiance is the product of the directional irradiance¹³ and the solid angle subtended by the aperture $\delta\omega$. The directional irradiance is the sum of the attenuated radiance of the surface and atmospheric path radiance. The general image-forming equation is

$$E_i(x_i, y_i) = [L_t(\mathbf{r}_t, \mathbf{r}_m)T_u(\mathbf{r}_t, \mathbf{r}_m) + L_p(\mathbf{r}_t, \mathbf{r}_m)]\delta\omega, \quad (1)$$

where $E_i(x_i, y_i)$ = the sensor irradiance at image coordinates (x_i, y_i)

$L_t(\mathbf{r}_t, \mathbf{r}_m)$ = the radiance of the imaged surface element (called target) in the direction of the sensor;

$T_u(\mathbf{r}_t, \mathbf{r}_m)$ = the atmospheric transmission from the target to the sensor;

$L_p(\mathbf{r}_t, \mathbf{r}_m)$ = the atmospheric radiance introduced in the path between the target and the sensor;

- \mathbf{r}_t = the position of the target in a global coordinate system;
- \mathbf{r}_m = the position of the sensor in the global coordinate system; and
- $\delta\omega$ = the solid angle subtended by the sensor aperture.

(The above equation represents intensity only; polarization is ignored in this paper.) Although one necessarily works with the sensor signal from which image irradiance can be computed, the subsequent discussion is more concerned with the radiance components that constitute the directional irradiance. The term sensor radiance will be used below to denote this directional irradiance:

$$L_m(\mathbf{r}_t, \mathbf{r}_m) = \frac{E_i(x_i, y_i)}{\delta\omega} = L_t(\mathbf{r}_t, \mathbf{r}_m)T_u(\mathbf{r}_t, \mathbf{r}_m) + L_p(\mathbf{r}_t, \mathbf{r}_m). \quad (2)$$

1. Target Radiance

The target radiance $L_t(\mathbf{r}_t, \mathbf{r}_m)$ depends on the photometric properties of the surface and the distribution of the illumination. Surface photometry is described by the bidirectional reflectance-distribution function (BRDF) $f_r(\mathbf{r}_t; \theta_i, \phi_i; \theta_r, \phi_r)$, where (θ_i, ϕ_i) and (θ_r, ϕ_r) , respectively, specify the angles of energy incidence and emittance.¹³ The illumination is a complex combination of attenuated solar irradiance, diffuse sky and cloud irradiance, and reflected ground radiance. Any of these elements may be missing due to shadowing.

2. Transmission

The reflected target radiance is attenuated by its passage from the target at \mathbf{r}_t to the satellite at \mathbf{r}_m by a transmission factor $T_u(\mathbf{r}_t, \mathbf{r}_m)$. The transmission is easily expressed as a function of optical thickness τ , which is a measure of the extinction properties (scattering and absorption) of the light path

$$T_u(\mathbf{r}_t, \mathbf{r}_m) = \exp[-\tau(\mathbf{r}_t, \mathbf{r}_m)],$$

where $\tau(\mathbf{r}_t, \mathbf{r}_m)$ is the optical thickness between the two points \mathbf{r}_t and \mathbf{r}_m . Transmission appears explicitly here as affecting only the target radiance, although it implicitly appears in the expressions for sky and sun irradiance of the target.

3. Path Radiance

The path radiance $L_p(\mathbf{r}_t, \mathbf{r}_m)$ includes light from outside the target that is scattered into the sensor path so as to appear to come from the target. Such atmospheric radiance is made of of light reflected from the ground outside the target (the background), a portion of the solar beam passing through the target-sensor path, and multiply scattered skylight. The path radiance does not include light from clouds that obscure part of the scene, a problem which is better handled as a modification to the scene rather than a property of the light path.

B. Simplifications

The sensor radiance equation in the form of Eq. (2) represents an extremely general formulation of the radiative transfer problem. Since the goal here is to

invert this equation to obtain a measure of surface reflectance in terms of sensor radiance, a more simplified equation is required. Several basic assumptions make the equation mathematically tractable. Other quite liberal assumptions are made in lieu of more detailed information about the particular application domain and result in an equation that depends on only six parameters.

First, the atmosphere is assumed to be a semi-infinite plane-parallel horizontally homogeneous air mass. Variations occur only in the z direction (vertical). Specific contributions to the radiative behavior due to multiple scattering and absorption are ignored. By adopting a phenomenological model based on empirically determined parameters, the major influences of these effects are incorporated as part of the aggregate behavior. The radiance from clouds is ignored.

Second, the target surface is assumed to be illuminated only by (1) a distant point sun of extraterrestrial irradiance E_0 whose incident rays make an angle θ_0 with the zenith, and (2) a uniform hemispherical sky (see the following paragraph). Illumination of a target by reflected ground radiance (as one side of a valley lit by the other side) is ignored. Without loss of generality, it is also assumed that the satellite sensor is a distant point directly over the scene.

Third, it is assumed that the distribution of sky radiance can be replaced by an equivalent uniform distribution, in the sense of producing the same irradiance on the target. This assumption permits an analytic expression for sky irradiance on target surfaces that are not horizontal and therefore see only a portion of the sky. Evaluation of the expression is straightforward^{14,15}:

$$E_{\text{sky}}(\mathbf{r}_t) = E_s(z)h(\theta_n, \phi_n) = E_s(z)^{1/2}(1 + \cos\theta_n),$$

where $E_s(z)$ is the sky irradiance on an unobstructed horizontal surface at elevation z , and $h(\theta_n, \phi_n) = 1/2(1 + \cos\theta_n)$ is the factor by which this irradiance is diminished for a surface whose normal makes an angle θ_n with the zenith. The function h has no azimuthal dependence although the argument ϕ_n is retained for generality.

Fourth, the earth's surface is assumed to reflect according to Lambert's law, where the albedo is allowed to vary from point to point. The radiance of a Lambertian surface is independent of the observation angle and depends only on the total irradiance and the surface albedo (bihemispherical reflectance ρ).¹³ The BRDF in this case is

$$f_r(\mathbf{r}_t; \theta_i, \phi_i; \theta_m, \phi_m) = \frac{\rho(\mathbf{r}_t)}{\pi}.$$

Such a model of earth reflectance has been popular in many investigations, even though its appropriateness has been seriously questioned.¹⁶ It is adopted here for three reasons. First, since the reflectance of a Lambertian surface is completely characterized by its albedo ρ , it is possible to compactly represent reflectance as an image, where intensity is proportional to albedo. Second, the sensor radiation equation is easily inverted for

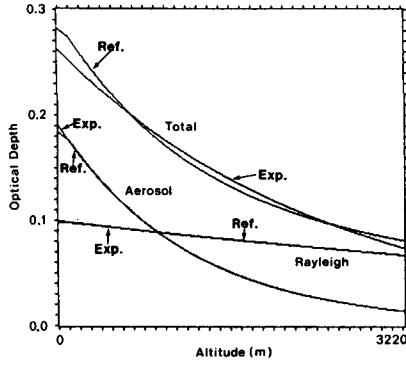


Fig. 1. Comparison of the two scattering components of a reference atmosphere (labeled *Ref.* in the figure) and their sum to exponential functions (labeled *Exp.*) derived from least-squares fitting. The parameters of the exponentials are given in the text.

a Lambertian reflector. Third, for applications of the type considered in this paper, the ground cover is not known *a priori*. In lieu of more specific information on the geometric reflectance properties of the viewed scene, a Lambertian surface is assumed. The problem of determining the local albedo remains.

Under the conditions and assumptions stated above, Eq. (2) becomes

$$L_m(x_t, y_t) = \frac{\rho(x_t, y_t)}{\pi} T_u(z) [E_0 T_d(z) R(\theta_n, \phi_n) + E_s(z) h(\theta_n, \phi_n)] + L_p(z), \quad (3)$$

where $L_m(x_t, y_t)$ = the sensor radiance associated with the target at (x_t, y_t) ;

$\rho(x_t, y_t)$ = the albedo of the target at (x_t, y_t) ;

$T_u(z) = \exp[-\tau(z)]$, the vertical transmission from altitude z up to the sensor;

E_0 = the extraterrestrial solar irradiance on a surface oriented normally to the incident rays;

$T_d(z) = \exp[-\tau(z)/\cos\theta_0]$, the slant-path transmission from sun to altitude z ;

$R(\theta_n, \phi_n)$ = a function that captures the geometric dependence of the BRDF and shadow information;

$E_s(z)$ = the sky irradiance on a horizontal surface at altitude z ;

$h(\theta_n, \phi_n)$ = the geometric dependence of sky irradiance on surface orientation as described above;

$L_p(z)$ = the path radiance between the sensor and the surface at altitude z ;

and
 $\tau(z)$ = The optical depth from the sensor to altitude z .

Altitude is obtained from the digital elevation model $z = z(x_t, y_t)$ and slope and aspect from the digital slope model $\theta_n = \theta_n(x_t, y_t)$ and $\phi_n = \phi_n(x_t, y_t)$. The function $R(\theta_n, \phi_n)$ describes the foreshortening of the surface as seen by the sun and is zero if the target is shadowed:

$$R(\theta_n, \phi_n) = \begin{cases} 0, & \text{if target is self- or cast-shadowed,} \\ \cos\theta'_0, & \text{if } 0 \leq \theta'_0 \leq \pi/2, \end{cases}$$

where θ'_0 is the angle between the local surface normal (θ_n, ϕ_n) and the solar direction (θ_0, ϕ_0) :

$$\cos\theta'_0 = \cos\theta_n \cos\theta_0 + \sin\theta_n \sin\theta_0 \cos(\phi_n - \phi_0).$$

Equation (3) is easily inverted to obtain albedo, the only quantity depending explicitly on the target's (x, y) position:

$$\rho(x_t, y_t) = \frac{\pi[L_m(x_t, y_t) - L_p(z)]}{T_u(z)[E_0 T_d(z) R(\theta_n, \phi_n) + E_s(z) h(\theta_n, \phi_n)]}. \quad (4)$$

In applying this equation to a real image, the predicted radiance L_m is replaced by the radiance L computed from the recorded signal.

C. Exponential Forms

The choice of functions for optical depth, sky irradiance, and path radiance is an open question. In the experiments described below, τ , E_s , and L_p were taken to be independent exponential functions of altitude:

$$\tau(z) = \tau_0 \exp(-z/H),$$

$$L_p(z) = L_{p0} \exp(-z/H_p),$$

$$E_s(z) = E_{s0} \exp(-z/H_s),$$

where the sky irradiance E_s is on a horizontal target. The base constants τ_0 , E_{s0} , and L_{p0} and the scale heights H , H_s , and H_p were determined from the evaluation of synthetic albedo images as described below.

The choice of exponential functions was inspired by their simplicity and their good match to several theoretical forms advanced in the literature. Optical depth values computed by Valley¹⁷ for Rayleigh (pure molecular) and aerosol components of the atmosphere are shown in Fig. 1 as functions of altitude for the spectral band $0.5 \leq \lambda \leq 0.6 \mu\text{m}$. Superimposed on these curves are the respective best-fit (in the least-squares sense) exponential forms. The exponentials agree very well with the individual components. The third pair of curves is the sum of the Rayleigh and aerosol components and its best-fit exponential. The fit is not very good here since the Rayleigh and aerosol components have distinct characteristic (scale) heights. The best-fit exponential parameters are

Rayleigh:	$\tau_{0R} = 0.09917$	$H_R = 8232 \text{ m,}$
aerosol:	$\tau_{0A} = 0.19$	$H_A = 1211 \text{ m,}$
sum:	$\tau_0 = 0.2619$	$H = 2529 \text{ m.}$

Some justification for the use of exponential forms for sky irradiance is available in the literature. When optical depth is a single exponential function of altitude, assuming that sky irradiance varies exponentially with altitude is equivalent to assuming $\ln E_s$ varies linearly with $\ln \tau$. This hypothesis was examined using computation of sky irradiance values for a Rayleigh atmosphere from several published sources. Figure 2 shows the variation of $\ln(E_s/E_0)$ with $\ln \tau$ at sea level ($z = 0$) for $\lambda = 0.55 \mu\text{m}$ and an average ground albedo of $\bar{\rho} = 0.25$. It is easily discerned that the points fall fairly

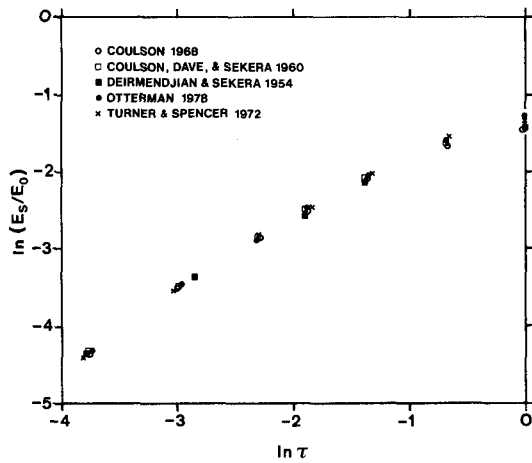


Fig. 2. Variation of relative sky irradiance values with optical depth for a Rayleigh atmosphere. The approximations made in the text amount to assuming a linear form for this variation. See notes for derivations: Coulson 1968,¹⁸ Coulson *et al.* 1960,¹⁹ Deirmendjian and Sekera 1954,²⁰ Otterman 1978²¹ Turner and Spencer 1972.^{22,23}

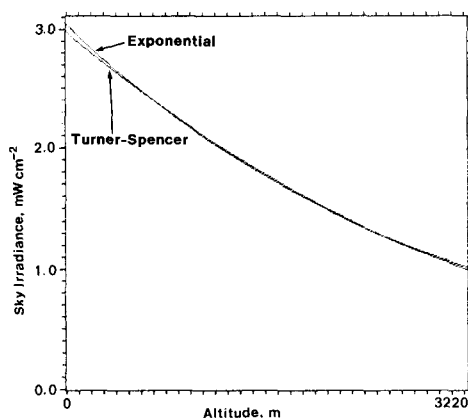


Fig. 3. Comparing sky irradiance on a horizontal surface as a function of altitude for the Turner-Spencer model²² and the exponential approximation thereof at $\lambda = 0.55 \mu\text{m}$. The calculation for the Turner-Spencer curve used a forward-scattering coefficient $\eta = 0.796$, average background albedo $\bar{\rho} = 0.15$, and a Rayleigh single-scattering phase function. The exponential curve $E_s(z) = E_{s0} \exp(-z/H_s)$ was fit by least-squares to yield $E_{s0} = 3.04 \text{ mW cm}^{-2}$ and $H_s = 2944.9 \text{ m}$.

close to a straight line, particularly within the range of optical depths expected in mountainous terrain, say, from $\ln\tau = -2.3$ to $\ln\tau = -0.49$ for the case of a Rayleigh atmosphere and an altitude range of from $z = 0 \text{ m}$ to $z = 4000 \text{ m}$.

Figure 3 exhibits the closeness of an exponential fit more directly. Here the Turner-Spencer formulation of sky irradiance for a mixed Rayleigh and aerosol atmosphere²² is compared to a best-fit exponential function of altitude. The agreement is excellent.

A similar if less satisfactory justification can be found for path radiance. Figure 4 shows data for $\ln(\pi L_p/E_0)$ vs $\ln\tau$ computed from three published sources, again for $\lambda = 0.55 \mu\text{m}$ and $\bar{\rho} = 0.25$, in the zenith direction for a sea-level target. The three sets do not agree as readily as the five sky irradiance sets. Within the interesting

range of $\ln\tau$, however, each set of values is approximately linear. Again, an exponential form for path radiance will fit the Turner-Spencer theoretical form for a combined Rayleigh and aerosol medium very well (Fig. 5).

III. Description of the Test Area

The region selected for the research lies in southwestern Switzerland, between $7^\circ 1'$ and $7^\circ 15'$ E and $46^\circ 8' 30''$ and $46^\circ 21' 5''$ N. The region, map titles Dent de Morcles and Les Diablerets, has been used in previous studies.^{24,25} A digital elevation model (DEM) was obtained as an array of 174×239 values on a 100-m grid digitized from contour maps. The vertical quantization is 10 m. Altitudes in the scene range from 410 m in the valley of the Rhone River (southeast corner of the area) to 2310 m on the Sommet des Diablerets (northeast

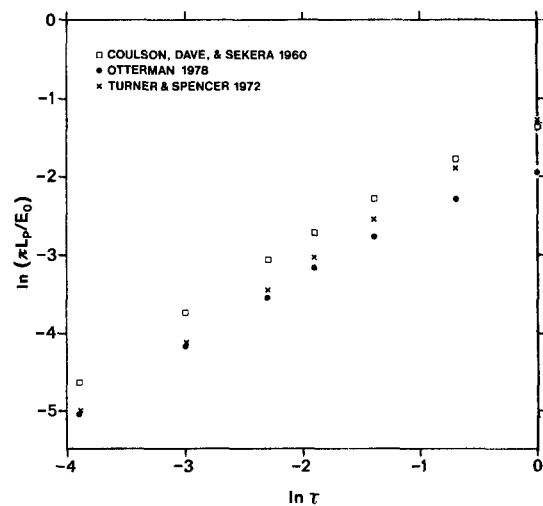


Fig. 4. Variation of relative path radiance values with optical depth in a Rayleigh atmosphere. The approximations made in the text amount to assuming a linear form for this variation. See notes for derivations: Coulson *et al.* 1960,¹⁹ Otterman 1978,²¹ Turner and Spencer 1972.^{22,23}

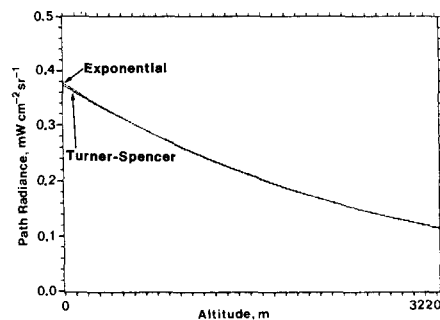


Fig. 5. Comparing path radiance as a function of altitude for the Turner-Spencer model²² and the exponential approximation thereof at $\lambda = 0.55 \mu\text{m}$. The calculation for the Turner-Spencer curve used a forward-scattering coefficient $\eta = 0.796$, average background albedo $\bar{\rho} = 0.15$, and a Rayleigh single-scattering phase function. The exponential curve $L_p(z) = L_{p0} \exp(-z/H_p)$ was fit by least-squares to yield $L_{p0} = 0.376 \text{ mW cm}^{-2} \text{ sr}^{-1}$ and $H_p = 2732.56 \text{ m}$.

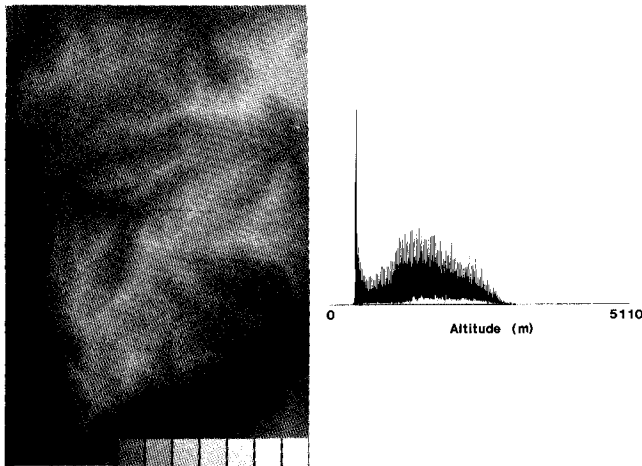


Fig. 6. Digital elevation model of the Dent de Morcles test region is displayed here as an image. Elevation is encoded as brightness, the brighter the area, the higher it is. The figure to the right is a histogram of elevation values, 0 m on the far left, 5110 m on the far right. The lowest point in the scene is 410 m, the highest is 3210 m. The peculiar disparity of adjacent altitudes in the histogram is an artifact of the process used to interpolate elevations during digitization of the contour maps (even altitudes were favored over odd ones). There are two histograms here: the smaller shaded one represents shadowed targets and the larger solid one sunlit targets (see text).

corner). A model of local slopes was generated from the DEM by modified first differences,²⁶ providing the slope θ_n and aspect ϕ_n for each target in the scene.

Figure 6 is an image of the area generated by translating altitude into brightness, accompanied by a histogram of altitudes present in the DEM. North is up in the photograph. The solid histogram represents targets that are sunlit, while the shaded one below represents targets that are shadowed. This distinction between sunlit and shadowed targets proved useful during the construction of albedo images described below. (In this particular histogram, the solid upper portion has many spikes, giving it a shaded appearance. This is an artifact of the process used to interpolate elevations during digitization of the contour maps, where even altitudes were favored over odd ones and thus appear more often.) The top of the solid histogram gives the total number of targets at a given altitude. The number of sunlit targets is the difference between that value and the top of the shaded histogram.

A multispectral image consisting of four spectral bands from Landsat 1 was obtained for the given area. The image, number 1078-09555, was acquired ~9:55 a.m. GMT on 9 Oct. 1972. For the experiments described below, only MSS band 4 (0.5–0.6 μm) was used, where the influence of the atmosphere is greater than in the other bands. During the overflight, the sun was at an elevation of 34.2° with an azimuth of 154.8° , corresponding to an incident solar direction (θ_0, ϕ_0) given by $\cos\theta_0 = \cos(90^\circ - 34.2^\circ) = 0.562$, $\phi_0 = 295.2^\circ$ counterclockwise from geographic east. The Landsat image was registered with the digital elevation model,²⁴ and radiometric corrections were applied to eliminate

striping.²⁷ Figure 7 shows the actual MSS band 4 as used in the experiments. Cast shadow information for the given sun position was generated by the application of a hidden surface display algorithm.²⁸ The resulting shadow masks, one for cast shadows and one for self-shadows, are shown in Fig. 8. Figure 9 is a synthetic image of the area created from the digital elevation model. The image shows how the surface would appear at the time of the overflight if the surface were a perfect Lambertian reflector of unit albedo and there were no intervening atmosphere.²⁶

IV. Determining Equation Parameters

A. Calibration Targets

The task of determining the parameters for the albedo equation would be relatively easy if there were suitable calibration points in a given satellite image. For example, Ahern *et al.*³⁰ describe the use of clear lakes as calibration targets to determine path radiance. Since the lakes have very low albedo, the sensor radiance recorded over them is essentially all path radiance. This technique can be profitably applied in mountainous terrain, provided a number of clear lakes appear over a wide range of altitudes in the scene. A regression analysis applied to the recorded sensor signals would yield a set of best-fit parameters for path radiance. Indeed, in the ideal case, six independent sensor radiance values from targets of known elevation, orientation, and albedo should be sufficient to determine all six model parameters.

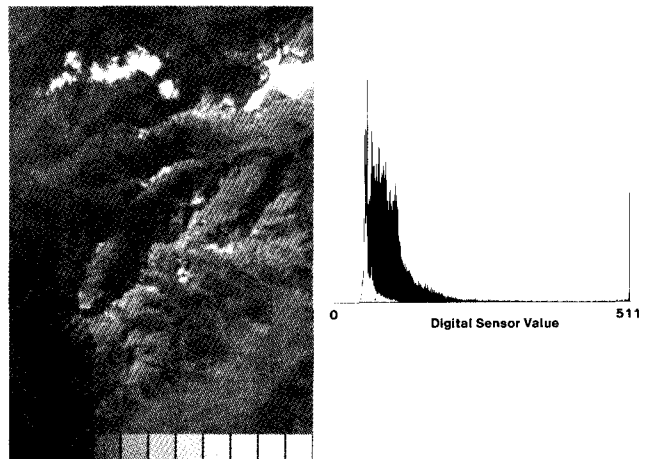


Fig. 7. Landsat 1 multispectral scanner image for the yellow-green channel 4, 500–600 nm. The original raw image was destriped and rectified to be commensurate with the digital terrain models as described in the text. Note the presence of clouds in the upper left corner of the image and the pronounced hazy appearance due to atmospheric path radiance. The histogram records digitized image brightness. A value of 0 corresponds to a sensor radiance of $0.0 \text{ mW cm}^{-2} \text{ sr}^{-1}$. A value of 511 corresponds to a sensor radiance of $2.48 \text{ mW cm}^{-2} \text{ sr}^{-1}$. (As provided on computer compatible tape, Landsat MSS channels 4, 5, and 6 are represented by 7-bit bytes, channel 7 by 6-bit bytes. These data were scaled to 9-bit bytes during destriping and rectification, hence the maximum value of 511.) The peak at the high end of the histogram is due to saturation on clouds and snow.

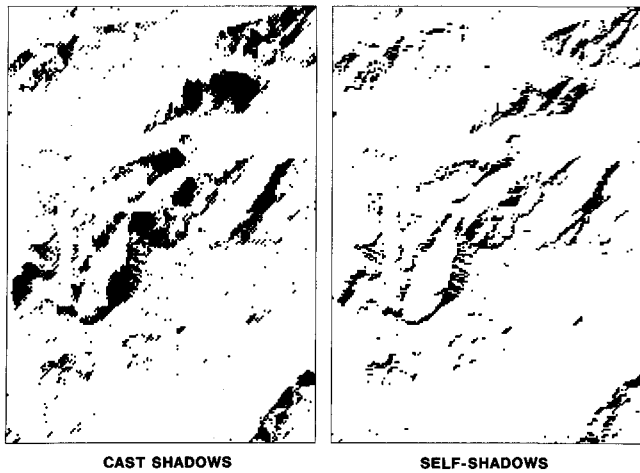


Fig. 8. Figure on the left is a binary map of those targets in the Dent de Morcles region that were in cast shadow under the illumination conditions of the Landsat overflight. The figure on the right is a binary map of those targets determined to lie in self-shadow (oriented away from the sun) under the given illumination. The shadow computation was performed using a method derived from hidden-surface plotting.^{28,29}

Regrettably, the Dent de Morcles region did not satisfy this rather stringent requirement. There were few lakes of sufficient clarity and they were not distributed throughout the scene's elevation range, a situation not uncommon in mountainous regions. No other targets of known albedo (for example, large areas of blacktop or dark tilled soil) were present.

B. Role of Shadows

On the other hand, the Landsat image contained a large number of shadowed areas that could be exploited as calibration targets. Shadows are especially attractive in that they exist at nearly every altitude in mountainous terrain and can provide elevation-dependent information. They are prevalent in Landsat images due to the early morning overflight and consequent low sun elevation. Piech and Schott³¹ used shadows advantageously in densitometric studies of specular and diffuse reflection from lake surfaces. They found a linear relationship between the scene radiance from sunlit areas and that from areas in cast shadow. From the relationship's slope and intercept values they were able to recover path radiance over the lakes as well as sky irradiance. There was no attempt to compare lake surfaces at different altitudes or nonhorizontal surfaces. In more recent work, Woodham²⁹ has examined the differences between sunlit and shadowed targets in Landsat images of a lake and a flat area of coniferous forest in British Columbia. He exhibited altitude profiles of sensor radiance that clearly showed a regular variation of path radiance with altitude. This variation can be exploited to help find path radiance.

C. Determining Optical Depth

The most satisfactory way of determining optical depth is through direct measurements of transmission at various altitudes. Such measurements were not available, however, for the experimental area on the

date the Landsat image was made. In lieu of site-specific data, published tables of Rayleigh and aerosol optical depth were used¹⁷ at least initially. In practice, an exponential form fitted to the altitude profiles of the sum of the two components was used, as described above.

D. Determining Path Radiance

The regular variation in sensor radiance pointed out by Woodham can be used to obtain information about path radiance. The scattered points in Fig. 10 comprise an altitude profile of the minimum sensor radiance over the test region. These minima occur almost entirely in shadowed targets. If one assumes that the minimum radiances are from shadowed targets with very small albedo, this profile approximates the path radiance function $L_p(z)$. One can determine a pair of values for the parameters L_{p0} and H_p by fitting an exponential curve to the profile. Two similar exponential curves are superimposed on the minimum sensor radiance profile in Fig. 10.

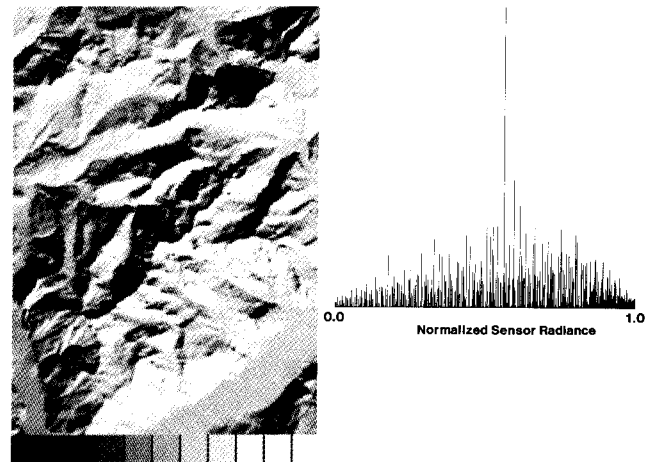


Fig. 9. Synthetic image of the test region with the sun in the same position as during the Landsat overflight. The ground is assumed to be a Lambertian reflector of uniform albedo $\rho = 1$. No atmosphere is assumed. The peak in the center of the histogram is from radiances within the Rhone Valley (the nearly uniform gray area at bottom right), a relatively flat region of almost constant altitude. The peak at the extreme left of the histogram is zero radiance for all shadows.

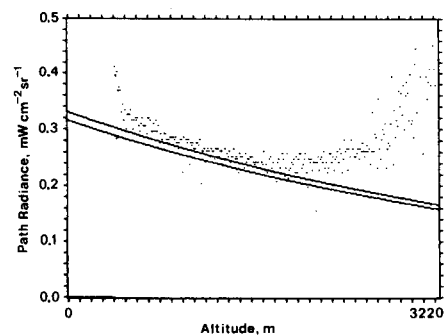


Fig. 10. Two possible exponential models of path radiance as inferred from minimum sensor data $L_p(z) = L_{p0} \exp(-z/H_p)$, where each curve was fitted manually to the data. For the upper curve, $L_{p0} = 0.33 \text{ mW cm}^{-2} \text{ sr}^{-1}$; for the lower curve, $L_{p0} = 0.315 \text{ mW cm}^{-2} \text{ sr}^{-1}$. $H_p = 4720 \text{ m}$ for both curves.

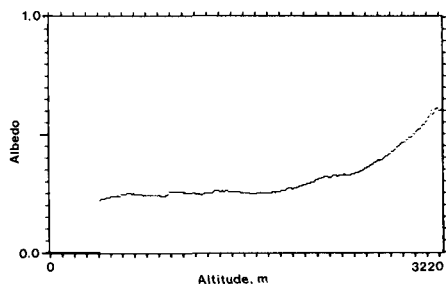


Fig. 11. Altitude profile of average albedo from sunlit targets in the Dent de Morcles test area. Albedo was calculated by assuming no intervening atmosphere and examining only sunlit targets at all altitudes. In such targets, reflected solar irradiance generally dominates, and computed albedo should approximate the true value. The data have been smoothed but show a distinct increase of albedo with altitude.

One must be careful when fitting model path radiance curves to the minimum sensor data. The model function is exponential, decreasing monotonically with altitude. Although the data points in Fig. 10 clearly drop off with elevation in the early part of the graph, the trend reverses at higher z . This trend is not too surprising, since the average albedo increases with altitude due to the presence of snow. Even in shadow, the minimum radiance is substantial. This increase is exhibited in Fig. 11, where the average albedo for all sunlit targets was computed by subtracting path radiance and ignoring sky irradiance. The high albedo of snow means that reflected skylight and the effects of mutual illumination cannot be neglected. When fitting the model curve it is necessary to use sensor radiances from targets only up to some arbitrary maximum altitude, discarding those beyond. In doing this, however, one also discards information about the behavior of $L_p(z)$ at higher altitudes that may be needed to find H_p .

Fitting path radiance to minimum sensor data requires satisfying physical constraints as well as choosing the data carefully. The exponential curves must lie entirely below the sensor radiance values, except for noise, since path radiance cannot be negative. One cannot therefore just fit an exponential through the data by least-squares. The two curves of Fig. 10 were both fitted by hand. The leftmost sensor data points in the figure stand markedly above the curve and were ignored in fitting the curve. There were few targets at this altitude extreme, all of which, on closer examination, lay near a shadow boundary in a river. It is likely that these targets actually contributed some sun glint and were thus brighter than expected.

One could argue that a line will fit the altitude profile as well as the displayed exponentials. Certainly, any of a host of functions would be suitable, but exponentials were chosen here for the reasons stated earlier.

E. Determining Sky Irradiance

Sky irradiance estimates and their variation with altitude are very hard to make. The presence of snow-covered targets in shadow suggests one method. If suitable optical depth and sensor radiance models are

assumed and snow albedo is estimated at perhaps 0.90, a very coarse value for E_s can be obtained for a target at altitude z with sensor radiance L :

$$E_s(z) \approx \frac{\pi[L - L_p(z)]}{\rho T_u(z)h(\theta_n, \phi_n)},$$

where $h(\theta_n, \phi_n) = \frac{1}{2}(1 + \cos\theta_n)$, the geometric factor for a hemispherical sky, $\rho = 0.90$, and $T_u(z)$ and $L_p(z)$ are presumed known. If several such values are obtained over a range of altitudes, E_{s0} and H_s can be estimated.

However, estimates obtained in the way described were not reliable. The exponential optical depth (Rayleigh and aerosol) described above and both path radiance curves shown in Fig. 10 were adopted to compute approximate sky irradiance. The values obtained were particularly sensitive to variations in $L_p(z)$ since the term $[L - L_p(z)]$ is usually small. They also depend on knowing $h(\theta_n, \phi_n)$ accurately. It was not discovered until late into the research that the digital terrain model had errors in many parts, including the even-altitude artifact shown in Fig. 6. These errors were magnified in the digital slope model. As a result, the method of estimating sky irradiance suggested here was not especially useful.

V. Subjective Evaluation of Albedo Images

The success of any method depends heavily on the quality of the data used. Although the determination of path radiance parameters from the minimum scene radiance profiles generates reasonable values, no such procedure is possible for the sky irradiance parameters. Estimates of sky irradiance for shadowed snow-covered targets depend strongly on the accuracy of surface slope, as well as the accuracy of the path radiance model and the assumption of the hemispherical nature of the sky. As mentioned above, the slope model was not reliable in many areas of the scene. Furthermore, because the satellite image had been resampled during rectification, the sensor values for nearby sunlit and shadowed targets were smeared together. Since noisy conditions are the rule rather than the exception in remote sensing, a better method was sought to determine the parameters of optical depth and sky irradiance.

The scarcity of reliable particulars about the imaged scene prompted an alternative procedure based on trial and error. One makes an educated guess at the atmospheric model parameter values and generates an albedo image using these values. By applying a set of subjective criteria, the acceptability of the image as an albedo map is determined. One can then refine the model parameter values, generate another image, and reapply the criteria. This process, while admittedly involving a bit of art, has been found to produce acceptable albedo maps.

A. Criteria for Judging Albedo Image

An albedo image ideally represents the spatial variation of surface albedo over the scene and is invariant with respect to the imaging situation and surface topography. To judge the quality of albedo maps gen-

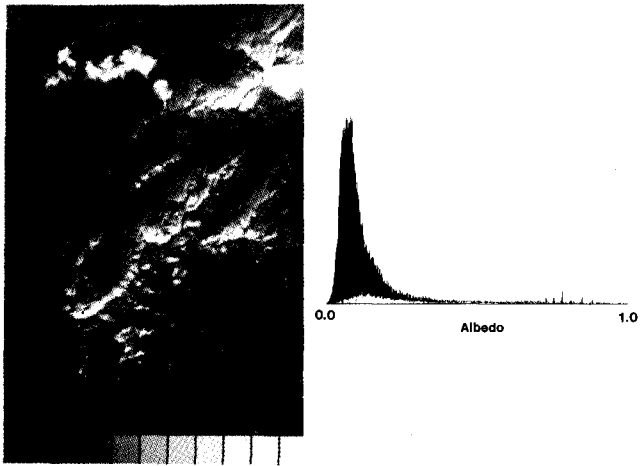


Fig. 12. Albedo image, and its associated histogram, generated using model parameters for exponential approximations to functional forms of path radiance and sky irradiance computed from the Turner-Spencer model:

$$\begin{aligned} \tau_0 &= 0.26185, & L_{p0} &= 0.376 \text{ mW cm}^{-2} \text{ sr}^{-1}, & E_{s0} &= 3.04 \text{ mW cm}^{-2}, \\ H &= 2529 \text{ m}, & H_p &= 2734 \text{ m}, & H_2 &= 2945 \text{ m}. \end{aligned}$$

The average computed albedo for sunlit targets was $\bar{\rho} = 0.117$ and for shadowed targets $\bar{\rho} = 0.276$.

erated as described above, three subjective criteria were established.

(1) There should be no visible evidence of surface shape (topography) that results from the imaging process. One expects the ground cover to change with elevation as the nature of the surface material changes. On occasion, it may even change with surface aspect (azimuth of the surface normal); for example, vineyards tend to be planted on south-facing slopes more than north-facing. But there should be no shading difference between targets of like albedo and different orientations.

(2) The computed albedo of sunlit and adjacent shadowed targets should be comparable, with no evidence of shadows. This is especially true if the shadow is cast by some nearby topographic feature. The boundary of such a shadow arbitrarily cuts across a region that is typically more or less homogeneous, that is, of similar elevation, surface slope, and ground cover on both sides of the boundary. A substantial deviation in albedo is probably due to an inaccurate atmospheric model, although bad image and topographic data also contribute.

(3) The dynamic range of the set of computed albedo for a scene ought to be reasonable. If the sensor radiance equation and the model underlying it were exact and the data were precise and error-free, every albedo calculated would lie between 0.0 and 1.0. Unfortunately, such ideal conditions are rarely realized in practice. A certain percentage of targets will have apparent albedo outside the physically possible range. The remainder should be distributed mostly within the range expected for natural surfaces of the kind being

observed, a few percent for clear lakes and dark fields or dense forest and perhaps 85–95% for snow-covered slopes.

B. Example Albedo Images

The above criteria were used to judge synthetic albedo images generated for a number of parameter sets, of which only three are presented here. The differences between acceptable albedo images were often quite subtle, and it was thought they would not survive the reproduction process. However, the difference between the albedo image and the original Landsat multispectral image is substantial. In all experiments, an extraterrestrial solar irradiance of $E_0 = 17.7 \text{ mW cm}^{-2}$ was assumed for MSS channel 4.^{32,33}

For comparison, the first albedo image is based on the Turner-Spencer calculations of path radiance and sky irradiance.²² Since no visibility measurements were available for the Dent de Morcles test area, from which aerosol optical depth is often inferred, the exponential forms fitted to Valley's molecular and aerosol optical depths¹⁷ were used. From these, the Turner-Spencer coefficient for forward scattering is

$$\eta = \frac{0.5\tau_R + 0.95\tau_A}{\tau_R + \tau_A} = 0.796,$$

where $\tau_R = 0.09917$ and $\tau_A = 0.19$. (Using Valley's sea-level numbers directly results in $\eta = 0.792$, a difference of only a half-percent.) Scattering was presumed to be dominated by the molecular component and a Rayleigh single-scattering phase function was used. The average background albedo $\bar{\rho}$ is 0.15. Albedo was computed from Eq. (4) using the exponential forms fitted to the Turner-Spencer model (shown in Fig. 5 for path radiance and Fig. 3 for sky irradiance).

There are several noteworthy features of the albedo image made using this model (Fig. 12). Certain areas that appear quite bright in the original Landsat MSS band 4 image are muted in the albedo image. This is particularly so for the snow-covered mountains in the northeast (upper left) corner and of the clouds in the northwest corner. It is unfortunate but well-known that the MSS sensors aboard Landsat satellites saturate on snow, clouds, and other highly reflective surfaces in sunlight. In the conditions assumed for the present research, this saturation means that targets with an albedo greater than ~ 0.8 would be indistinguishable in the original MSS image. The recorded radiances for high-albedo targets such as snow and clouds are less than they should be, and the computed albedo is too low.

A second fact is that it is quite easy to distinguish shadowed from sunlit areas. The shadowed areas are brighter, that is, have a higher apparent albedo than neighboring regions in sun. This is emphasized in the histogram to the right of the image, where the peak for shadowed targets lies to the right of the peak for sunlit targets, although it is not as pronounced. This difference is clear in the enclosed valley in the left center of the image. The cast shadow boundary running through the middle separates sun on the left from shadow on the

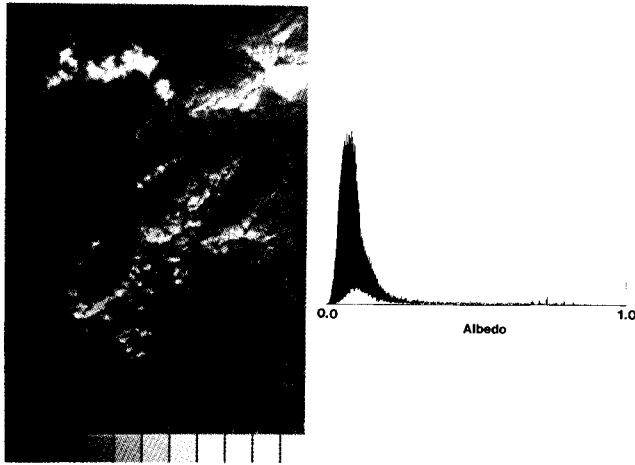


Fig. 13. Improved albedo image and its associated histogram. Albedo was computed using the following atmospheric model parameters:

$$\begin{array}{lll} \tau_0 = 0.26185, & L_{p0} = 0.315 \text{ mW} & E_{s0} = 3.0 \text{ mW} \\ & \text{cm}^{-2} \text{ sr}^{-1}, & \text{cm}^{-2} \\ H = 2529 \text{ m}, & H_p = 4720 \text{ m}, & H_s = 4720 \text{ m}. \end{array}$$

The average computed albedo for sunlit targets was $\bar{\rho} = 0.110$ and for shadowed targets $\bar{\rho} = 0.200$.

right. This visible distinction between shadows and sunlit areas violates the second of the criteria set forth above for an acceptable albedo map. It is possible to improve the image by adjusting the six model parameters appropriately.

The third feature of interest, and one that suggests how to modify the model parameters, is the apparent increase with elevation of albedo in shadows. The northwest-facing slopes of the southeast ridge bounding the central valley lie in shadow. Near the valley center, the computed albedo is ~ 0.25 – 0.30 . It increases with elevation (and with slope) to 0.80 – 0.90 just below the ridge crest. This contrasts with the opposite side of the valley, where the sunlit southeast-facing slopes show no such differential: the albedo has a more or less uniform value of 0.20 – 0.30 . A similar phenomenon can be seen in the vicinity of the summit of Dent de Morcles and other places in the image.

The albedo map also reveals an artifact due to the presence of clouds in the image. Since the sensor radiance model ignores clouds and cloud shadows, the albedo computed for targets obscured by clouds are too high and those computed for targets lying in cloud shadows are too low. This is evident in the upper left corner of the image, the cloud shadow lying slightly above and to the left of the bright area that is the cloud.

Other apparent artifacts are the isolated very bright or very dark targets scattered about the image. It is unlikely that these are due to aliasing, since resampling of the image during rectification would have blurred them over several adjacent targets. It is most probable that these isolated events result from either: (1) an

incorrect indication of shadow, for example, a sunlit target may in fact be shadowed or vice versa; or (2) an incorrect surface orientation computed from an inaccurate digital slope model. The latter would be most noticeable in shadowed targets and in sunlit targets that are near grazing solar incidence.

One clarification should be made in passing. Although saturation of the MSS sensor over high-albedo areas such as snow and clouds in principle means that no target should have a computed albedo > 0.8 , higher values will result due to errors in calculated surface orientation or shadow status. Such targets are revealed in the histogram of Fig. 12, where the rightmost bin contains a very large number of shadowed targets. (A computed albedo of greater than unity was clamped to 1.0 before generating the albedo image and histogram.)

The behavior of the computed albedo in shadow in Fig. 12 suggests that the elevation dependence of the path radiance or sky irradiance components or both may be wrong. The generally larger shadow albedo indicates that perhaps too little path radiance is being removed. A larger value would reduce shadow albedos while affecting sunlit target albedo less (the relative contribution to sky radiance of reflected sunlight is about twice that of path radiance for a horizontal surface under the conditions assumed here). By increasing the scale height H_p , the path radiance is made larger at higher elevations.

A similar argument applies to sky irradiance. By increasing the scale height H_s , the irradiance from skylight becomes larger with altitude and results in smaller computed albedo. The ratios of reflected skylight to path radiance to reflected sunlight for the conditions assumed here are $\sim 2:5:9$, respectively. Increasing sky irradiance therefore makes only a small difference in most computed sunlit albedo values, while substantially decreasing those for shadowed targets.

A second albedo image was generated from a different set of parameters (Fig. 13). A single exponential optical depth function derived from Valley's data as described earlier was used. Both the sea-level value L_{p0} and scale height H_p for path radiance were taken from the exponential model fitted to minimum scene radiances as discussed above. Sea-level sky irradiance was arbitrarily set at 3.0 mW cm^{-2} , a value slightly under the Turner-Spencer value used in the first albedo image. Lacking other data, sky irradiance scale height was taken to be the same as for path radiance.

The appearance of this image is better than that of the first one. Shadowed areas more closely match adjacent sunlit areas. The histogram of shadow albedo more closely parallels that of sunlit albedo. However, there is still marked disparity between the two. Furthermore, there is some evidence that the albedo gradient observed on shadowed northeast-facing slopes may actually be a property of the scene. The division between the brighter, higher area and the darker valley floor is fairly distinct, and each area appears approximately homogeneous. The larger albedo may indicate the presence of moderately reflective surface material

such as unvegetated rock, perhaps interspersed with snow. The south-facing slope is exposed to more sun and may support more vegetation and less snow. This is one example of an aspect-dependent effect that should be preserved in the albedo image, since it is actually a property of the surface.

The parameter values used to obtain the albedo image of Fig. 13 can be varied somewhat without significantly changing the appearance of the image. Another very similar appearing albedo image was generated from a moderately different set of parameter values (Fig. 14). Sea-level path radiance was increased to a value between that of the two preceding models in an effort to decrease shadow albedo over that computed in the second model. To partially compensate for reducing the sunlit albedo, sea-level optical depth was decreased, while scale height was increased. The change in optical depth in effect simulated a clearer atmosphere (less aerosol) than Valley's reference atmosphere.

This last albedo image is subtly different from the second one in appearance, but the histograms of the two differ enough to favor this last one. If one compares the albedo image in Fig. 14 with the synthetic image in Fig. 9, it is apparent that virtually all shading due to varying topography has been obliterated. The match between sunlit and shadowed target albedo is very good. One notes that the boundaries between sun and shadow are evident as strings of dark targets. These result from inaccuracies in the digital elevation model used to calculate slopes and the locations of cast shadows. Finally,

the range of computed albedo fits well within the physically required range, for sunlit and shadowed targets individually and together, and their respective histograms agree well. Tuning the parameters further could undoubtedly improve the image slightly, but this was not done.

VI. Discussion

The simple model of sensor radiance advanced above is based on an engineering approach designed to expedite the extraction of useful data from images of mountainous terrain. In this regard, it enjoys several advantages. It is easily inverted to obtain albedo as a locally computable quantity. That is, the albedo of a surface target depends only on the target's own elevation, orientation, and sensor radiance and not that of other targets in the scene. It is computationally cheap to generate albedo images, providing fast feedback on the appropriateness of the model parameters. It depends on a minimum of site-specific data and therefore can be readily applied to existing images for which very little information on the atmospheric state is available. To be sure, a digital terrain model is required, but this is generally much easier to produce *post facto* than measurements of atmospheric state. The process of subjective evaluation allows one to develop an intuition for tuning if a small number of model parameters are used. Finally, by explicitly accounting for sky irradiance and path radiance it is possible to recover reflectance information from shadowed targets.

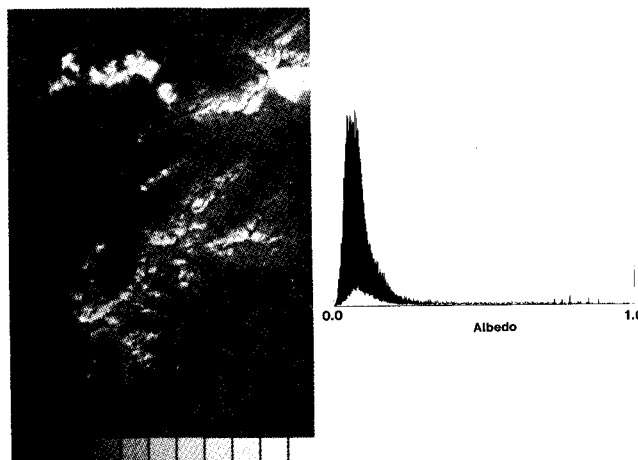


Fig. 14. Third example albedo image and its associated histogram. Albedo was computed using the following atmospheric model parameters:

$$\begin{array}{lll} \tau_0 = 0.23, & L_{p0} = 0.33 \text{ mW} & E_{s0} = 3.04 \text{ mW} \\ & \text{cm}^{-2} \text{ sr}^{-1}, & \text{cm}^{-2}, \\ H = 4000 \text{ m}, & H_p = 2734 \text{ m}, & H_s = 2945 \text{ m}. \end{array}$$

The average computed albedo for sunlit targets was $\bar{\rho} = 0.108$ and for shadowed targets $\bar{\rho} = 0.184$.

On the other hand, by adopting this simple model one abandons fidelity to actual environmental conditions. First, the atmosphere is not horizontally homogeneous. When combined with the spatial variation of surface reflectance across the scene, this inhomogeneity means that path and sky radiance depend on horizontal position as well as altitude. The effect can be significant even in flat terrain^{34,35} and is emphasized in mountainous areas, where large topographical features tend to decouple portions of the atmosphere.

Second, while it is conceivable that multiple scattering and absorption can be incorporated implicitly into the sensor radiance equation, neglect of the particulars of particle scattering lead to an incorrect treatment of, for example, sky irradiance. The hemispherical sky model used above ignores the increased radiance of the horizon sky. Targets inclined toward the horizon are therefore assumed to receive less sky irradiance than they really do, resulting in a larger computed albedo. The computation of shadow albedo is especially sensitive to this omission. The model also ignores the presence of the solar aureole that results from the preferentially forward-scattering atmospheric aerosols. Surfaces inclined toward the sun receive significantly greater sky irradiance than computed in the model here. However, this omission is not serious, since the aureole radiance ought to be included in the direct solar irradiance term.

Third, radiative transfer theory clearly shows that optical depth, path radiance, and sky irradiance are tightly coupled, a fact ignored here by the assumption of independent model parameters. A more careful choice of functional forms could exploit the constraints on the solution space afforded by this coupling. It was not considered appropriate for the current investigation as it would complicate the mathematics and would be difficult to evaluate. However, the introduction of optical depth as the coupling element between the atmospheric components is one refinement that should be fairly straightforward.

Fourth, the exponential dependence on altitude of the functions $\tau(z)$, $L_p(z)$, and $E_s(z)$ are not faithful to their respective behaviors in the real atmosphere, even though they agree with theoretical functional forms for a Rayleigh atmosphere. Recent measurements of aerosol scattering coefficients over Europe show they decrease slowly or are constant through an altitude of ~2300 m and decrease rapidly thereafter.^{36,37} For the experimental conditions here, this implies a split aerosol optical depth, linear at low altitude and dropping off perhaps exponentially at the upper elevations in the scene. Of course, the variation of this profile across the scene due to changing topography may be larger than the discrepancy between this split form and an exponential form.

Fifth, a digital terrain model gives information on the shape of the ground, not always on the shape of the overlying ground cover. In the case of a forest, for example, the tops of the trees are not constrained to follow the ground. Although this is a complication of remote imaging in general, it is particularly important in rugged terrain. The sensor radiance and albedo equations account for the shape of the imaged surface, which in this case is not necessarily that provided by the topographic model. On the other hand, the difference in target orientation this causes may be masked by even larger variations between the assumed Lambertian character of the reflection of light from trees and its true behavior.

In some respects, the departure of the model from real conditions is forced by the nature of the remote sensing problem addressed here. In particular, lack of *a priori* knowledge about the photometry of the surface was one reason cited for assuming a Lambertian surface. The reflectance of most of the earth's surface that has been measured shows strong anisotropy,³⁸ especially at low sun elevations.³⁹ The computation of albedo for sunlit targets ought to account more carefully for the incident solar direction in the function $R(\theta_n, \phi_n)$ in Eqs. (2) and (4). However, unless one already has some idea of the nature of the surface, a more complicated expression is not justified. Similarly, the expression for target irradiance does not include reflected ground radiance. Mutual illumination among targets can have a large effect as seen in Fig. 10 (if indeed that is a partial explanation for the rise in minimum sensor radiance with altitude), but to include it in the target irradiance integral presupposes knowledge of the albedo of the surrounding terrain.

The presence of sloping targets is a feature of rugged terrain that demonstrates the importance of modeling both sun and sky irradiance. For sunlit targets, the direct solar component generally contributes a substantially larger portion of total target irradiance than skylight. This is certainly true for low optical thickness, high sun elevation, and moderate surface slopes. However, even in clear atmospheres, when the target surface slopes away from the sun so as to be near grazing incidence, the solar and sky irradiance components are comparable. For medium to low sun elevations, the magnitude of the slope as measured by the angle θ_n is not that large. Under the sensor radiance model adopted here and using the model parameters for Fig. 14, the target irradiance from sun and sky are equal when the slope has the values in Table I. For surfaces facing directly away from the sun ($\phi_n - \phi_0 \approx 180^\circ$), a small slope will so increase the relative importance of skylight that it becomes the dominant irradiant.

A. Sensitivity Analysis

It is useful to briefly analyze the dependence of computed albedo on the model parameters to see how sensitive it is to the values of the model parameters. This gives some indication of the importance of each parameter in determining albedo.

Table I. Surface Slope Angle for Which the Direct Solar Contribution to Target Irradiance Equals the Diffuse Sky Contribution; Values are Given at Various Altitudes and Two Azimuthal Angles for the Atmospheric Model of Fig. 14

Alt. (m)	θ_n when $\phi_n - \phi_0 = 180^\circ$ (degrees)	θ_n when $\phi_n - \phi_0 = 90^\circ$ (degrees)
0	7	47
410	12	59
1000	17	69
2000	23	78
3210	27	83

Table II. Relative Sensitivities $(\partial\rho/\partial X)/(\rho/X)$ of Computed Albedo to the Path Radiance Model Parameters $X = L_{p0}$ and $X = H_p$ at Various Altitudes for MSS Band 4; Other Parameter Values are Those of Fig. 14; Model Sensor Radiance L Is in $\text{mW cm}^{-2} \text{sr}^{-1}$

Alt. (m)	$(L = 0.34)$		$X = (L = 1.41)$		$(L = 2.48)$	
	L_{p0}	H_p	L_{p0}	H_p	L_{p0}	H_p
0	-33.000	0.000	-0.306	0.000	-0.153	0.000
500	-4.218	-0.771	-0.242	-0.044	-0.125	-0.023
1000	-2.061	-0.754	-0.194	-0.071	-0.102	-0.037
1500	-1.277	-0.700	-0.156	-0.086	-0.083	-0.046
2000	-0.876	-0.641	-0.127	-0.093	-0.068	-0.050
2500	-0.637	-0.582	-0.104	-0.095	-0.056	-0.052

Table III. Relative Sensitivities $(\partial\rho/\partial X)/(\rho/X)$ of Computed Albedo to the Sky Irradiance $X = E_{s0}$ and $X = H_s$ and Optical Depth Model Parameters $X = \tau_0$ and $X = H$ for Horizontal Sunlit Targets at Various Altitudes for MSS Band 4; Other Parameter Values are Those of Fig. 14

Alt. (m)	$X =$			
	E_{s0}	H_s	τ_0	H
0	-0.278	0.000	0.526	0.000
500	-0.240	-0.041	0.477	0.060
1000	-0.207	-0.070	0.432	0.108
1500	-0.177	-0.090	0.390	0.146
2000	-0.151	-0.103	0.350	0.175
2500	-0.129	-0.109	0.314	0.196

Table IV. Relative Sensitivities $(\partial\rho/\partial X)/(\rho/X)$ of Computed Albedo to the Sky Irradiance $X = E_{s0}$ and $X = H_s$ and Optical Depth Model Parameters $X = \tau_0$ and $X = H$ for Horizontal Shadowed Targets at Various Altitudes for MSS Band 4; Other Parameter Values are Those of Fig. 14

Alt. (m)	$X =$			
	E_{s0}	H_s	τ_0	H
0	-1.000	0.000	0.230	0.000
500	-1.000	-0.170	0.203	0.025
1000	-1.000	-0.340	0.179	0.045
1500	-1.000	-0.509	0.158	0.059
2000	-1.000	-0.679	0.140	0.070
2500	-1.000	-0.849	0.123	0.077

Table II lists the relative sensitivities of computed albedo to changes in the two path radiance parameters for a low, a moderate, and a high sensor radiance value. The numbers in each column are the values of $(\partial\rho/\partial X)/(\rho/X)$, where X is the model parameter heading the column. The sensitivities of the sky irradiance and optical depth parameters are listed in Tables III and IV, respectively, for horizontal sunlit and shadowed targets. The sensitivities were computed for the set of parameter values used to generate the albedo image in Fig. 14.

Not surprisingly, the relative effects of each of optical depth, path radiance, and sky irradiance drop off with altitude as the atmosphere diminishes. This is reflected by the decreasing values of τ_0 , L_{p0} , and E_{s0} . The dependence on the scale heights H , H_p , and H_s , however, increases with altitude (it is proportional to the ratio of z to the scale height). This emphasizes the importance of using the radiance from high-altitude targets to help determine the scale heights. As mentioned above, the use of minimum sensor radiance to find a form for $L_p(z)$ suffers, in this experimental situation at least, from the inability to use the higher elevation information.

It appears that the computation of albedo of a sunlit target is overall most sensitive to changes in the optical depth parameters, except for targets of low sensor radiance at low altitude. For shadows, on the other hand, computed albedo is most sensitive to changes in sky irradiance and to path radiance at very low sensor values and low altitudes. But the sensitivity to changes in optical depth is still very important for shadow albedos.

VII. Conclusions

It is evident that the albedo images generated above are more meaningful representations of intrinsic surface properties than the original satellite image. An honest evaluation of their worth requires at least comparing the computed albedo maps to ground truth for the experimental area or examining the output of an automated classification program given an albedo map as input. Unfortunately, the former evaluation was not possible in the present investigation since no ground truth was available, and the latter was not attempted due to time constraints. Nonetheless, several facts emerge from the experiments performed in the course of the research.

(1) It is especially important to model terrain and atmospheric effects in mountainous areas for three reasons: (a) to recover the reflectance of shadowed targets they must be identified and sky irradiance must be adequately modeled; (b) the variation of ground slope must be accounted for in both the solar and sky irradiance components, and these two effects are comparable for targets near grazing incidence; (c) the path radiance varies with altitude across the scene and must be modeled carefully to obtain reflectance in targets of low sensor radiance (such as those in shadow and on steep slopes).

(2) A simple model of sensor radiance can approximate atmospheric effects well enough to generate reasonable, simple representations of surface reflectance for mountainous terrain. Values of the model parameters can be obtained by trial generation of albedo images and subsequent subjective evaluation.

(3) The albedo image represents surface reflectance (under the Lambertian assumption) in a simple form immediately comprehensible to a human evaluator. It is therefore a useful tool in determining how the model parameters should be set to obtain an acceptable albedo map.

(4) Although the presence of specific calibration targets in the scene would simplify the determination of parameter values, shadows may be used almost as effectively. Path radiance as a function of altitude can be computed this way. But subjective evaluation is still necessary to assist in finding suitable values for the other components, especially sky irradiance.

(5) The sensor radiance model is generally most sensitive to changes in the optical depth parameters, except at low sensor radiances. It is expected that a more realistic form of optical depth as a function of altitude, including a proper account of the coupling among transmission, path radiance, and sky irradiance, would benefit the albedo computation even if other simplifying assumptions were unchanged.

The engineering method presented in this paper illustrates the limitations in recovering surface reflectance strictly from the image-forming equation. A coarse model of surface and atmospheric effects was assumed here in order to find which aspects are most important in mountainous terrain. As seen, a coarse model leads to coarse results. A more refined approach would furnish a more satisfying analytic procedure than the subjective method discussed above; however, it might require considerably more detailed input than is generally available. At one extreme, an exact model of the radiative transfer process would paradoxically require an exact description of surface reflectance before it could be solved to find surface reflectance. It is clear that human image analysts do not dynamically solve the radiative transfer equation when interpreting images but apply more intelligent techniques. Until such techniques are better understood, one must be content with improving the satellite image by filtering it to remove influences—such as topographic and atmospheric effects—that are not part of the desired reflectance information.

This paper is a revised version of a dissertation submitted by R.W.S. to the Department of Electrical Engineering and Computer Science, MIT, in May, 1981, in partial fulfillment of the requirements for the degree of Master of Science. The research described herein was done at the Artificial Intelligence Laboratory of the Massachusetts Institute of Technology. Support for the Laboratory's artificial intelligence research is provided in part by the Defense Advanced Research Projects Agency under Office of Naval Research contract N00014-80-C-0505.

The authors would like to thank Kurt Brassel for providing the original digital terrain model of the Dent de Morcles and Les Diablerets regions, Robert J. Woodham for timely comments and criticism, and J. M. Brady for useful comments on the paper. An unknown referee is appreciatively acknowledged for his studied review of the original manuscript and the many excellent criticisms and comments that resulted. R.W.S. especially thanks B.K.P.H. for supervising the present research and for many useful discussions and encouragement.

References

1. S. I. Solomon, J. Cameron, J. Chadwick, and A. S. Aggarwal, in *Proceedings Second Symposium on Machine Processing of Remotely Sensed Data* (Laboratory for Applications of Remote Sensing, Purdue U., West Lafayette, Ind. 1975), p. 4B-1.
2. R. M. Hoffer and staff, *Natural Resource Mapping in Mountainous Terrain by Computer Analysis of ERTS-1 Satellite Data*, LARS Info Note 061575, (Laboratory for Applications of Remote Sensing, Purdue U., West Lafayette, Ind., 1975); also available from NTIS as N76-14567.
3. M. D. Fleming, J. S. Berkebile, and R. M. Hoffer, in *Proceedings, Second Symposium on Machine Processing of Remotely Sensed Data* (Laboratory for Applications of Remote Sensing, Purdue U., West Lafayette, Ind., 1975), p. 1B-54.
4. F. G. Sadowsky and W. A. Malila, "Investigation of Techniques for Inventorying Forested Regions. Vol. 1: Reflectance Modeling and Empirical Multispectral Analysis of Forest Canopy Components," Final Report, NASA-CR-151561 (1977); also available from NTIS as N73-14462.
5. B. N. Holben and C. O. Justice, *Photogramm. Eng. Remote Sensing* **46**, 1191 (1980).
6. J. N. Howard and J. S. Garing, *Trans. Am. Geophys. Union* **52**, 371 (1971).
7. E. J. McCartney, *Optics of the Atmosphere: Scattering by Molecules and Particles* (Wiley, New York, 1976).
8. G. V. Rozenberg, *Sov. Phys. Usp.* **3**, 346 (1960).
9. A. J. LaRocca and R. E. Turner, "Atmospheric Transmittance and Radiance: Methods of Calculation," IRIA State-of-the-Art Report, ERIM 107600-10-T (Environmental Research Institute of Michigan, Ann Arbor, 1975); also available from NTIS as AD-A017 459.
10. S. Chandrasekhar, *Radiative Transfer* (Dover, New York, 1960).
11. S. Ueno, H. Kagiwada, and R. Kalaba, *J. Math. Phys.* **12**, 1279 (1971).
12. G. I. Marchuk *et al.*, *The Monte Carlo Methods in Atmospheric Optics* (Springer, Berlin, 1980).
13. F. E. Nicodemus *et al.*, "Geometrical Considerations and Nomenclature for Reflectance," *Nat. Bur. Stand. U.S. Monogr.* **160** (1977).
14. P. Moon, *Illum. Eng.* **37**, 707 (1942).
15. B. K. P. Horn and R. W. Sjoberg, *Appl. Opt.* **18**, 1770 (1979).
16. J. A. Smith, T. L. Lin, and K. J. Ranson, *Photogramm. Eng. Remote Sensing* **46**, 1183 (1980).
17. S. L. Valley, *Handbook of Geophysics and Space Environments* (McGraw-Hill, New York, 1965).
18. K. Coulson, *J. Atmos. Sci.* **25**, 759 (1968). Sky irradiance data for $\mu_0 = \cos\theta_0 = 0.562$ were interpolated from the published tables for a surface albedo of A (or $\bar{\rho}$) = 0.25. $E_s(\tau) = F_s + F_d$ of the published data, where the value for F_d for $A = 0.25$ was interpolated from the values for $A = 0.20$ and $A = 0.30$.
19. K. L. Coulson, J. V. Dave, and Z. Sekera, *Tables Related to Radiation Emerging from a Planetary Atmosphere with Rayleigh Scattering* (U. California Press, Berkeley, 1960). Sky irradiance data were obtained by numerically integrating the tabulated values of downward radiance for $\mu_0 = \cos\theta_0 = 0.6$ and A (or $\bar{\rho}$) = 0.25. Path radiance data were obtained from the tabulated values of upward radiance at $\mu_0 = \cos\theta_0 = 0.6$ and $A = 0.25$ by first subtracting the reflected target radiance. The reflected target radiance is $L_t = (T_d E_0 \mu_0 + E_s) A / \pi$.
20. D. Deirmendjian and Z. Sekera, *Tellus* **6**, 382 (1954). Sky irradiance data for $\mu_0 = \cos\theta_0 = 0.562$ at A (or $\bar{\rho}$) = 0.25 were interpolated from the published values of $\mu_0 = 1.0, 0.6, 0.1$ at $A = 0.25$.
21. J. Otterman, *Appl. Opt.* **17**, 3431 (1978). Sky irradiance values for $\mu_0 = 0.562$ and $\bar{\rho} = 0.25$ were computed directly from the published formula for a Rayleigh atmosphere. Otterman fails to give an explicit formula for path radiance (which would be inappropriate for his approach) but does give one for radiant exitance. The plotted path radiance value is actually the radiant exitance at $\mu_0 = 0.562$ and $\bar{\rho} = 0.25$ divided by 2π .
22. R. E. Turner and M. M. Spencer, in *Proceedings, Eighth International Symposium on Remote Sensing of the Environment* (Environmental Research Institute of Michigan, Ann Arbor, 1972), pp. 895-934.
23. Sky irradiance and path radiance data were obtained directly from the published formula for a Rayleigh atmosphere with $\bar{\rho} = 0.25$ and $\mu_0 = 0.562$.
24. B. K. P. Horn and B. L. Bachman, *Commun. Assoc. Comput. Mach.* **21**, 914 (1978).
25. R. J. Woodham, "Looking in the Shadows," Working Paper 169 (Artificial Intelligence Laboratory, MIT, 1978).
26. B. K. P. Horn, *Proc. IEEE* **69**, 14 (1981).
27. B. K. P. Horn and R. J. Woodham, *Comput. Graphics Image Process.* **10**, 69 (1979).
28. R. J. Woodham, "Two Simple Algorithms for Displaying Orthographic Projections of Surfaces," Working Paper 126 (Artificial Intelligence Laboratory, MIT, 1976).
29. R. J. Woodham, *Proc. Soc. Photo-Opt. Instrum. Eng.* **238**, 361 (1980).
30. F. J. Ahern, D. G. Goodenough, S. C. Jain, and V. R. Rao, in *Proceedings, Eleventh International Symposium on Remote Sensing of the Environment* (Environmental Research Institute of Michigan, Ann Arbor, 1977), pp. 731-755.
31. K. R. Piech and J. R. Schott, *Proc. Soc. Photo-Opt. Instrum. Eng.* **51**, 84 (1974).
32. M. P. Thekaekara, *J. Environ. Sci.* **13**, 6 (1970).
33. J. Otterman and R. S. Fraser, *Remote Sensing Environ.* **5**, 247 (1976).
34. R. E. Turner, "Radiative Transfer in Real Atmospheres," Technical Report ERIM 190100-24-T (Environmental Research Institute of Michigan, Ann Arbor, 1974); also available from NTIS as N74-31873.
35. R. E. Turner, "Atmospheric Effects in Multispectral Remote Sensor Data," Technical Report ERIM 109600-15-F (Environmental Research Institute of Michigan, Ann Arbor, 1975); also available from NTIS as N75-26474.
36. W. S. Hering, "An Operational Technique for Estimating Visible Spectrum Contrast Transmittance," Scientific Report 16 (Visibility Laboratory, Scripps Institution of Oceanography, La Jolla, Calif., 1981).
37. R. W. Johnson and J. I. Gordon, "Airborne Measurements of Atmospheric Volume Scattering Coefficients in Northern Europe, Summer 1978," Scientific Report 13 (Visibility Laboratory, Scripps Institution of Oceanography, La Jolla, Calif., 1980).
38. B. W. Fitch, *J. Atmos. Sci.* **38**, 2717 (1981).
39. B. Brennan and W. R. Bandeen, *Appl. Opt.* **9**, 405 (1970).